The Astrophysical Journal, 732:76 (14pp), 2011 May 10 doi:10.1088/0004-637X/732/2/76
© 2011. The American Astronomical Society. All rights reserved. Printed in the U.S.A.

PAndAS' PROGENY: EXTENDING THE M31 DWARF GALAXY CABAL*

Jenny C. Richardson[1], Mike J. Irwin[1], Alan W. McConnachie[2], Nicolas F. Martin[3], Aaron L. Dotter[4], Annette M. N. Ferguson[5], Rodrigo A. Ibata[6], Scott C. Chapman[1], Geraint F. Lewis[7], Nial R. Tanvir[8], and R. Michael Rich[9]

[1] Institute of Astronomy, Madingley Road, Cambridge, CB3 0HA, UK; jcr@ast.cam.ac.uk
[2] NRC Herzberg Institute for Astrophysics, 5071 West Saanich Road, Victoria, British Columbia, V9E 2E7, Canada
[3] Max-Planck-Institut für Astronomie, Königstuhl 17, D-69117 Heidelberg, Germany
[4] Space Telescope Science Institute, 3700 San Martin Drive, Baltimore, MD 21218, USA
[5] Institute for Astronomy, University of Edinburgh, Royal Observatory, Blackford Hill, Edinburgh, EH9 3HJ, UK
[6] Observatoire de Strasbourg, 11, rue de l'Université, F-67000, Strasbourg, France
[7] Institute of Astronomy, School of Physics, University of Sydney, NSW 2006, Australia
[8] Department of Physics and Astronomy, University of Leicester, University Road, Leicester LE1 7RH, UK
[9] Department of Physics and Astronomy, Physics and Astronomy Building, 430 Portola Plaza, Box 951547, University of California, Los Angeles, CA 90095-1547, USA

Received 2010 August 26; accepted 2011 February 12; published 2011 April 19

ABSTRACT

We present the discovery of five new dwarf galaxies, Andromeda XXIII–XXVII, located in the outer halo of M31. These galaxies were discovered during the second year of data from the Pan-Andromeda Archaeological Survey (PAndAS), a photometric survey of the M31/M33 subgroup conducted with the MegaPrime/MegaCam wide-field camera on the Canada–France–Hawaii Telescope. The current PAndAS survey now provides an almost complete panoramic view of the M31 halo out to an average projected radius of ∼150 kpc. Here we present for the first time the metal-poor stellar density map for this whole region, not only as an illustration of the discovery space for satellite galaxies, but also as a birds-eye view of the ongoing assembly process of an L_* disk galaxy. Four of the newly discovered satellites appear as well-defined spatial overdensities of stars lying on the expected locus of metal-poor ($-2.5 < [\mathrm{Fe/H}] < -1.3$) red giant branch stars at the distance of M31. The fifth overdensity, And XXVII, is embedded in an extensive stream of such stars and is possibly the remnant of a strong tidal disruption event. Based on distance estimates from horizontal branch magnitudes, all five have metallicities typical of dwarf spheroidal galaxies ranging from $[\mathrm{Fe/H}] = -1.7 \pm 0.2$ to $[\mathrm{Fe/H}] = -1.9 \pm 0.2$ and absolute magnitudes ranging from $M_V = -7.1 \pm 0.5$ to $M_V = -10.2 \pm 0.5$. These five additional satellites bring the number of dwarf spheroidal galaxies in this region to 25 and continue the trend whereby the brighter dwarf spheroidal satellites of M31 generally have much larger half-light radii than their Milky Way counterparts. With an extended sample of M31 satellite galaxies, we also revisit the spatial distribution of this population and in particular we find that, within the current projected limits of the PAndAS survey, the surface density of satellites is essentially constant out to 150 kpc. This corresponds to a radial density distribution of satellites varying as r^{-1}, a result seemingly in conflict with the predictions of cosmological simulations.

Key words: galaxies: dwarf – galaxies: structure – Local Group

Online-only material: color figures

1. INTRODUCTION

The last decade has seen tremendous advances in our understanding of our nearest giant neighbor, M31. A particular highlight has been the first detailed exploration of the outer halo of the galaxy. The Isaac Newton Telescope wide-field imaging survey of M31 mapped a $\sim 100 \times 100$ kpc^2 region down to $\approx$3 mag below the red giant branch (RGB) tip and revealed a strikingly complex picture of an inner halo replete with stellar substructure (Ibata et al. 2001; Ferguson et al. 2002; Irwin et al. 2005), and led to the discovery of Andromeda XVII (Irwin et al. 2008). With no sign of the substructure abating at the survey edge, attention naturally turned to the more remote regions of the M31 halo. Using MegaCam on the Canada–France–Hawaii Telescope (CFHT), Ibata et al. (2007) mapped the stellar distribution in the entire southeastern quadrant in the radial range ∼30–150 kpc, with an extension toward M33. A rich array of tidal streams and overdensities, globular clusters, and satellite galaxies were revealed. Encouraged by the success of these surveys we embarked on the Pan-Andromeda Archaeological Survey (PAndAS; McConnachie et al. 2009), a large program using the CFHT MegaCam imager to map the entire stellar halos of both M31 and M33 out to distances of ∼150 and ∼50 kpc, respectively.

As the data came in, quadrant by quadrant, increasing numbers of new dwarf spheroidal (dSph) satellite galaxies were revealed in the outskirts of M31: And XI, XII, XIII, XV, XVI, XVIII, XIX, XX, XXI, and XXII (Martin et al. 2006; Ibata et al. 2007; McConnachie et al. 2008; Martin et al. 2009). In parallel efforts, the existence of And IX, X, and XIV was discovered by other groups (Zucker et al. 2004, 2007; Majewski et al. 2007). The recently acquired second year of data for the PAndAS survey now yields an almost complete perspective of the outer halo of M31 out to ∼150 kpc, showing for the first time the full structural complexity of the ongoing assembly process

* Based on observations obtained with the MegaPrime/MegaCam, a joint project of the Canada–France–Hawaii Telescope (CFHT) and CEA/DAPNIA, at CFHT which is operated by the National Research Council (NRC) of Canada, the Institut National des Science de l'Univers of the Centre National de la Recherche Scientifique (CNRS) of France, and the University of Hawaii.

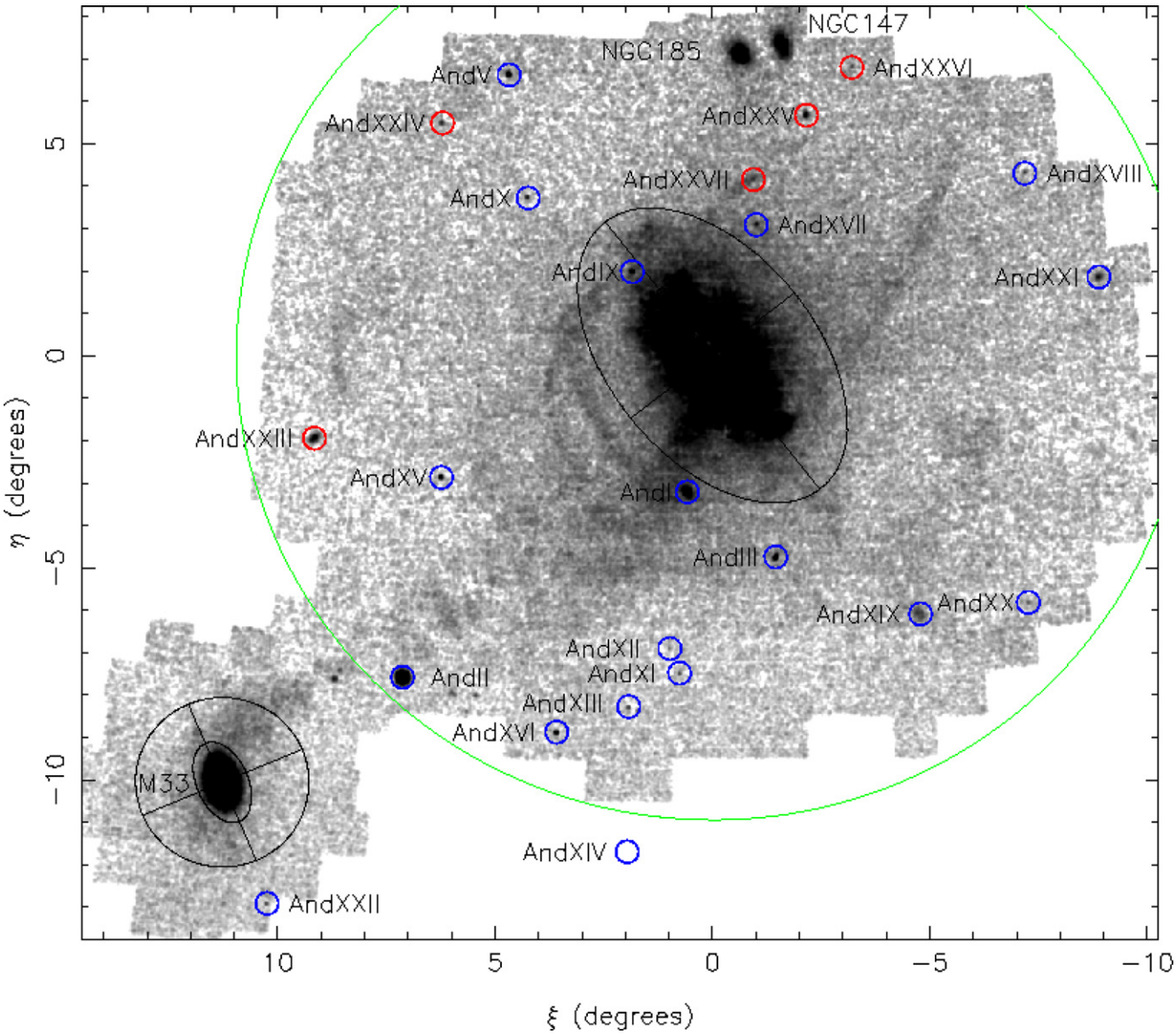

Figure 1. Surface density map of stars with colors and magnitudes consistent with belonging to metal-poor red giant branch populations at the distance of M31. The almost uniform underlying background is mainly contributed by foreground stars in the Milky Way together with a small residual contamination from unresolved compact background galaxies. All of the previously known M31 dwarf spheroidals in this region covered by the survey are readily visible as well-defined overdensities and are marked with blue circles. The five new dwarf spheroidals are highlighted in red. (And XIV is the dwarf spheroidal just south of the present survey area, while And VI and VII lie, respectively, well to the west and north of the region shown.) NGC147 and NGC185 appear at the top of the map and M33 at the bottom left. The green circle lies at a projected radius of 150 kpc from the center of M31 within which most of the survey lies. In addition to the satellite galaxies, numerous stellar streams and substructures are visible. Although the majority of small overdensities are satellite galaxies of M31, a few to the southern end of the map (not circled) are resolved globular cluster systems picked out surrounding nearby low-redshift background elliptical galaxies.

(A color version of this figure is available in the online journal.)

of an L_* disk galaxy (Figure 1). Also, clearly visible within this panoramic view are multiple dwarf galactic satellites in the M31 system including five new dwarf galaxies, And XXIII, And XXIV, And XXV, And XXVI, and And XXVII, revealed here for the first time (circled in red in Figure 1).

However, our knowledge of the satellite system of M31 is still limited. Current wide area ground-based photometric observations of satellites at the distance of M31 cannot easily reach much deeper than the horizontal branch (HB), limiting detection to objects at the bright end of the satellite luminosity function (LF; $M_V \lesssim -6.5$). If M31 had a population of ultra-faint dwarfs (UFDs) like the MW, they would not be picked up in present surveys. Spectroscopic observations are currently even more constrained and are limited in practice to the handful of brighter RGB stars close to the tip of the RGB (TRGB) or, if present, any bright asymptotic giant branch (AGB) stars. Despite these limitations, much can already be said of the generic properties of these new objects from the current photometric survey data alone.

The absolute magnitudes of the recently discovered M31 satellites range from $M_V = -6.4$ for And XII and And XX (Martin et al. 2006; McConnachie et al. 2008) to a surprisingly bright $M_V \lesssim -9.7$ for And XVIII (McConnachie et al. 2008), patently showing the incompleteness of the M31 satellite LF in regions that have so far only been surveyed with photographic plates. We note here that, even with hindsight, only one of these new discoveries (And XVIII) is visible on the earlier photographic sky surveys and none of the five new satellites

presented here are visible on earlier sky surveys either. With their relative faintness and significant sizes (half-light radii >100 pc), these new systems are usually assumed to be (dSph) galaxies, i.e., devoid of any significant amount of gas and without significant recent star formation. The absence of gas is currently consistent with the results of H I surveys, but the upper limits on their H I content generally remain relatively high, (2–3) $\times$ 10^5 $M_\odot$ (Grcevich & Putman 2009), though in some cases the H I limit is much tighter. For example, Chapman et al. (2007) constrained the H I mass of And XII to be $<3 \times 10^3$ $M_\odot$. In general, however, it is currently not possible to rule out entirely that some of these galaxies may still contain non-negligible amounts of gas.

The properties of the surviving satellite populations of L_* galaxies, such as M31 and the MW, are presumably directly linked to the overall evolution and assembly of the host systems. Since M31 and the MW evolved in a common environment, and have similar morphological types (SbI-II and SbcI-II), masses ((1–2) $\times$ 10^{12} $M_\odot$; Evans & Wilkinson 2000), and luminosities, one would also expect their satellite systems to be similar. Intriguingly, a growing body of evidence suggests that this is not the case. McConnachie & Irwin (2006a) compared the structural properties of the then known MW and M31 dSph populations and found systematic differences whereby the dSphs of M31 had half-light radii typically twice as large as the MW dSph. As more dSphs have been discovered around both galaxies, Kalirai et al. (2010) and Collins et al. (2010) have used the kinematics of several M31 dSphs to show that the brighter dSphs are systematically dynamically colder and have lower central densities than their MW counterpart, while at the fainter end of the dSph LFs the structural properties appear to overlap (Kalirai et al. 2010). This potential luminosity-dependent discrepancy between the observed properties of the MW and M31 satellite systems is puzzling and as more satellites are discovered is worth reassessing.

In this paper, we analyze the properties of these new dwarfs and place them in the context of the rest of the Andromedan satellite galaxy population. Section 2 summarizes the PAndAS data and the processing steps involved. Sections 3 and 4 present the new systems and their structural properties, and in Section 5 we discuss them in the context of the ensemble of Andromeda satellites and compare this to the MW satellite system.

Throughout this paper, the distance modulus of M31 is assumed to be $(m - M)_0 = 24.47 \pm 0.07$, or 785 ± 25 (McConnachie et al. 2005).

2. THE PAndAS SURVEY

PAndAS builds upon the previous CFHT/MegaCam surveys of M31 presented in Martin et al. (2006), Ibata et al. (2007), and McConnachie et al. (2008), and we refer the reader to these papers for a full description of the observing strategy, data reduction, and data quality. The imaging was carried out with the MegaPrime/MegaCam camera mounted on the CFHT which has 36 2048 $\times$ 4612 CCDs with a pixel size of 0.187 arcsec and 1×1 deg^2 field of view. Although the survey is comprised of contiguous imaging, small gaps in exposures lead to a scientifically usable field of view of 0.96×0.94 deg^2 for each of the (currently 357) pointings of the survey. Each field has been observed in the MegaCam g and i filters for at least 1350 s, split into 3×450 s dithered sub-exposures. Good seeing ($<0\farcs8$) and rigorous CFHT on-site quality control ensures that the photometry reaches $g \sim 25.5$ and $i \sim 24.5$ with a signal-to-noise ratio (S/N) of 10. With data of this quality the star/galaxy separation only begins to degrade significantly at magnitudes fainter than this.

Data were preprocessed by the Elixir system at CFHT; this includes de-biasing, flat-fielding, and fringe-correcting the data as well as determining the photometric zero points. The data were then transferred to Cambridge where they were further processed using a version of the Cambridge Astronomical Survey Unit (CASU) photometry pipeline (Irwin & Lewis 2001) which was specially tailored to CFHT/MegaCam observations. Here, the astrometry of individual frames are refined and this information was used to register and then stack component images to create the final image products from which the survey catalogs are generated. Finally, the astrometry is further refined, and objects from the catalogues are morphologically classified (stellar, non-stellar, noise-like) before creating the final band-merged g and i products. The catalogs provide additional quality control information, and the classification step also computes the aperture corrections required to place the photometry on an absolute scale. The band-merged catalogs for each field are then combined to form an overall single entry g, i catalog for each detected object. In this process, objects lying within 1 arcsec of each other are taken to be the same, and the entry with the higher signal-to-noise measure is retained. Objects present only on g or i are retained throughout this process.

In the following, unless otherwise stated, the magnitudes are presented in their natural instrumental (AB) system without any reddening correction (g, i). When required for analysis, de-reddened magnitudes (g_0 and i_0) or reddened model isochrones have been determined from the Schlegel et al. (1998) $E(B-V)$ extinction maps, using the following correction coefficients: $g_0 = g - 3.793\,E(B-V)$ and $i_0 = i - 2.086\,E(B-V)$ listed in their Table 6.

3. THE PAndAS METAL-POOR STELLAR DENSITY MAP

The spectacular results of the PAndAS survey are shown in Figure 1. The map details the density distribution of all candidate metal-poor stars in the stellar halos of M31 (M33) out to 150 kpc (50 kpc), covering more than 300 deg^2, or around 55,000 kpc^2 at the distance of M31. Here, stars are considered as metal-poor candidates if they lie in the locus of the color–magnitude diagram (CMD) where RGB stars with metallicities of $\approx -2.5 <$ [Fe/H] < -1.3 fall if at the systemic distance of M31 $\pm$100 kpc, and have i-band and g-band magnitudes satisfying $21.0 < i < 24.0$ and $g < 25.0$. In this we are implicitly assuming that such stars belong to predominantly old ($\approx$10 Gyr) stellar populations.

This is the first time that a deep ($\Sigma_V \simeq 33$ mag arcsec^{-2}) high-resolution contiguous map of the majority of the extended stellar halo of any L_* galaxy has been observed. Since the signatures of past accretions and mergers are preserved for longer times in the outer regions of massive galaxies (e.g., Johnston et al. 1996), the PAndAS survey has effectively provided a unique insight into the accretion history of M31. Although the map presented in Figure 1 was optimized to search for dSph-like structures at the distance of M31, it also clearly reveals that M31 is looped by a series of giant stellar streams which have been torn off from accreted satellite galaxies, as well as other more diffuse stellar substructures. In particular, we note the great stellar arc to the northwest seen here for the first time, the two well-defined streams of stars crossing the southeast minor axis, and the diffuse debris apparently emanating from M33 that is visible over a large region indicative of a strong tidal interaction with M31 (see McConnachie et al. 2009). In

Table 1
Derived Properties of the Satellites

Parameter	And XXIII	And XXIV	And XXV	And XXVI	And XXVII
α (J2000)	$01^h29^m21\overset{s}{.}8 \pm 0\overset{s}{.}5$	$01^h18^m30\overset{s}{.}0 \pm 0\overset{s}{.}5$	$00^h30^m08\overset{s}{.}9 \pm 0\overset{s}{.}5$	$00^h23^m45\overset{s}{.}6 \pm 0\overset{s}{.}5$	$00^h37^m27\overset{s}{.}1 \pm 0\overset{s}{.}5$
δ (J2000)	$38°43'08'' \pm 10''$	$46°21'58'' \pm 10''$	$46°51'07'' \pm 10''$	$47°54'58'' \pm 10''$	$45°23'13'' \pm 10''$
(l, b) (°)	(131.0, −23.6)	(127.8, −16.3)	(119.2, −15.9)	(118.1, −14.7)	(120.4, −17.4)
$E(B-V)$[a]	0.066	0.083	0.101	0.110	0.080
$(m-M)_0$[b]	24.43 ± 0.13	23.89 ± 0.12	24.55 ± 0.12	24.41 ± 0.12	24.59 ± 0.12
D (kpc)	767 ± 44	600 ± 33	812 ± 46	762 ± 42	$\geqslant 757 \pm 45$
r_{M31} (kpc)	$\sim 126 \pm 44$	$\sim 197 \pm 33$	$\sim 97 \pm 47$	$\sim 101 \pm 42$	$\sim 86 \pm 48$
[Fe/H][c]	−1.8 ± 0.2	−1.8 ± 0.2	−1.8 ± 0.2	−1.9 ± 0.2	−1.7 ± 0.2
r_h(arcmin)	4.6 ± 0.2	2.1 ± 0.1	3.0 ± 0.2	1.0 ± 0.1	1.8 ± 0.3:
$r_h(pc)$	1035 ± 50	378 ± 20	732 ± 60	230 ± 20	455 ± 80:
ϕ (N to E) (°)	138 ± 5	5 ± 10	170 ± 10	145 ± 10	150 ± 10:
$\epsilon = 1 - b/a$	0.40 ± 0.05	0.25 ± 0.05	0.25 ± 0.05	0.25 ± 0.05	0.4 ± 0.2:
M_V	−10.2 ± 0.5	−7.6 ± 0.5	−9.7 ± 0.5	−7.1 ± 0.5	−7.9 ± 0.5
$\Sigma_{V,0}$ (mag arcsec^{-2})	28.0 ± 0.5	27.8 ± 0.5	27.1 ± 0.5	27.4 ± 0.5	27.6 ± 0.5

Notes. The errors quoted for the profile parameters derived in Section 4.1 ($\alpha, \delta, r_h, \phi$ and ϵ) are the 1σ errors from the marginalized likelihood contours of the grid search. Structural parameters derived for And XXVII are marked ":" to reflect the additional uncertainties caused by the presence of the intersection stellar stream.

[a] $E(B-V)$ interpolated from the Schlegel et al. (1998) dust maps.

[b] Due to the sparsity of the upper RGB, distance moduli are calculated from the magnitude of the horizontal branch from the deeper g-band data.

[c] The median metallicity of the metallicity distribution functions from Figure 5.

addition, numerous outer halo globular clusters are also being found, many coincident with these stream-like features (Mackey et al. 2010).

Interestingly, although part of the northwest arc was also seen by Tanaka et al. (2010), their stream "F," there is no evidence in our metal-poor map for any overdensity at the location of their stream "E," nor in any of our other maps made with different metallicity cuts.

Our panoramic view also offers the most complete picture of the dwarf satellite galaxy population of M31 to date. Previously known dSphs are circled in blue. The five new dSphs, which are the main subject of this paper, are circled in red. Of the 25 currently known Andromedan dSphs, And VI and VII lie well outside the field of view shown here, while And XIV lies just to the south of the surveyed region and is shown with a blue circle. Larger satellites of M31 such as M32 and NGC205 are hidden within the dense inner halo, but NGC147 and NGC185 make an appearance at the northern edge of the image. Including M31 and M33, but not 2 the numerous streams and other extended substructure, the number of galaxies in the Andromedan system comfortably visible in the surveyed area in this image totals 28. Since these objects are distributed all over the area surveyed with no obvious curtailment as a function of radius, it is clear that even this large-scale panoramic view is still not large enough to capture all the detail of the M31 outer halo systems.

4. ANDROMEDAS XXIII–XXVII

The five new dwarf galaxies were straightforward to detect as overdensities in the matched-filter surface density maps of metal-poor RGB stars. There are no other obvious candidate satellites visible in this map or in our equivalent average metallicity and metal-rich maps. For simplicity and following convention, we have named them Andromeda XXIII–XXVII (And XXIII–XXVII) after the constellation they are found in. As noted earlier, the locations of all previously known dSphs (blue circles) and the five new dwarfs (red circles) are readily visible in Figure 1. Moving from east to west (left to right in the figure), the new galaxies are And XXIII, And XXIV, And XXVII, And XXV, and And XXVI. Their central coordinates are listed in Table 1. A zoom-in view of the distribution of stars seen in each galaxy is shown in the left-hand panels of Figure 2 where the distributions of the candidate metal-poor RGB stars are highlighted with bolder dots. The other points plotted show the rest of the cataloged stellar population in these fields and serve to highlight where gaps in survey coverage might have an impact. The overlaid ellipses are set at twice the derived half-light radii and also use the ellipticity and position angle from the likelihood analysis (see Section 4.1). And XXIII–XXVII all appear as fairly obvious overdense concentrations of metal-poor stars in the localized spatial distribution maps.

CMDs of stars lying within two half-light radii of the center of each galaxy (within the ellipses in Figure 2; listed in Table 1) are plotted on the left-hand side of Figure 3 and are compared to CMDs of nearby reference regions of the same area (middle panel of Figure 3). These particular reference regions were generally defined using an elliptical annulus just beyond four half-light radii from the center of each dSph. However, for And XXVII, this region intersected too much of the enveloping northwest arc (stream) and an ellipse 5 arcmin to the south and west was used instead, though even here there is some contamination from stream stars. The dwarf galaxies exhibit clear RGB sequences with $0.8 \lesssim g-i \lesssim 1.5$ and $i \gtrsim 21.0$ which are either absent, or nothing like as apparent, in the reference regions. The narrow color width of the RGBs, typical of dSph galaxies, suggests that their stellar populations do not contain a wide range of metallicities. There is no evidence that any of these galaxies contains a young main-sequence population. Reference regions are mainly devoid of RGBs and all contain a "red cloud" of foreground dwarf stars from the Milky Way (MW) disk at the top right of the CMD with $g-i \gtrsim 2.0$ and $i \lesssim 23.0$. The fainter group of objects centered at $0.0 \lesssim g-i \lesssim 1.5$ and $i \gtrsim 24.0$ and most readily visible in some of the comparison regions are generally caused by contamination from misclassified compact background galaxies.

The right-hand panel of Figure 3 displays the i-band LFs of And XXIII–XXVII (black) computed within two half-light radii of the centers, and a scaled LF from a nearby reference

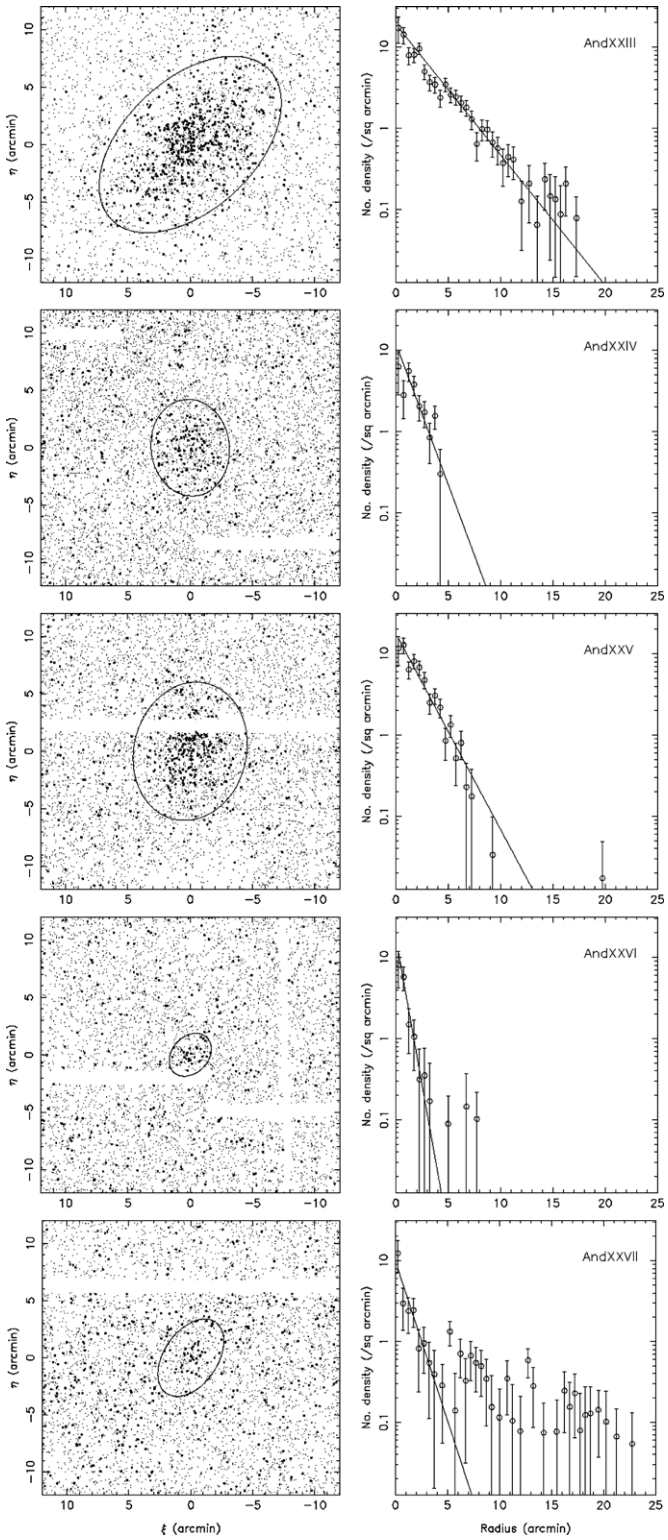

Figure 2. Left panels: the spatial distribution of stellar sources around And XXIII–XXVII. Small dots represent all stars in the PAndAS survey and large dots correspond to stars with colors and magnitudes consistent with metal-poor red giant branch populations at the distance of M31. The central ellipse in each region denotes two half-light radii for each dwarf galaxy using the structural parameters listed in Table 1. Right panels: background-corrected radial profiles of the dwarfs measured using the average stellar density within series of fixed elliptical annuli using the parameters from Table 1. Allowance is made for incompleteness due to CCD gaps and the edges of the survey. The error bars account for Poisson counting statistics and uncertainties in the derived background level. The overlaid curves are derived from the tabulated model parameters (Table 1) but are not direct fits to the data points.

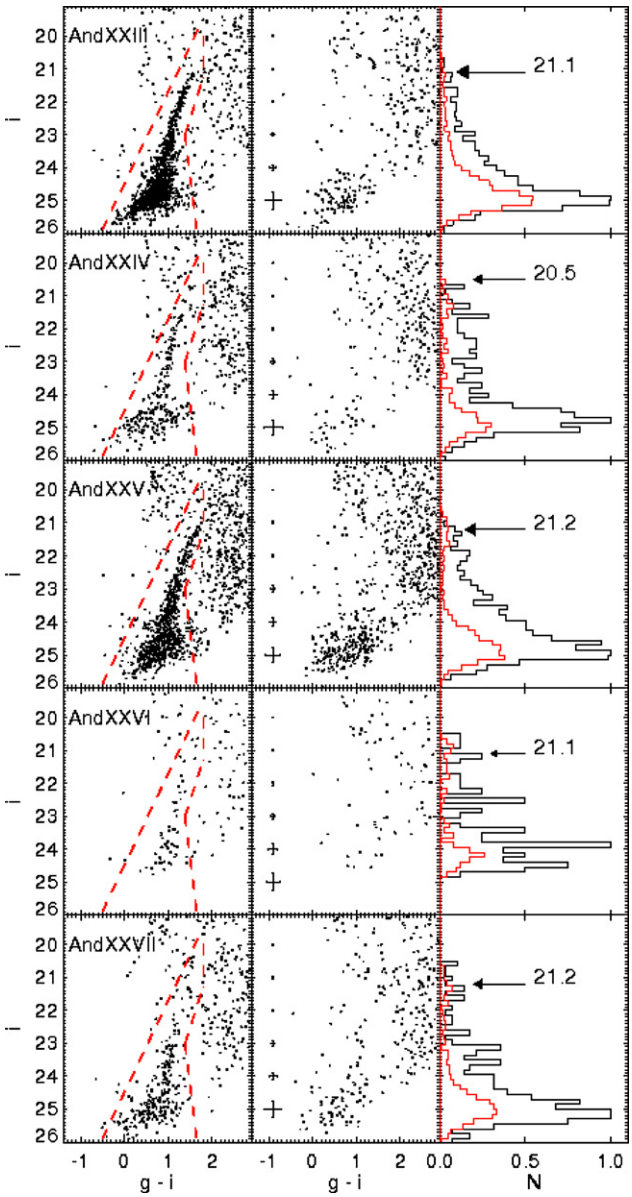

Figure 3. Left and center panels: color–magnitude diagrams within two half-light radii of And XXIII–XXVII and of suitable nearby comparison regions covering the same area after correcting for gaps in the survey coverage if required. In all cases a well-defined RGB is clearly visible as an overdensity of stars with $0.8 \lesssim g-i \lesssim 1.5$ and $i \gtrsim 21.0$ that does not have an equivalent presence in the reference CMD. The rms photometric errors in i and $g-i$ as a function of magnitude are displayed on the left-hand side of the center panel. Right panels: the i-band luminosity functions of the central regions of each dwarf (black) and a suitably scaled much larger neighboring comparison region (red). Only stars within the dashed polygons were included in the LFs, equivalent polygons were used to select stars from the reference fields. In most cases, the luminosity functions show a clear change in counts at the TRGB and the arrows mark the TRGB magnitudes predicted by our distance estimates (see Section 4.2).

(A color version of this figure is available in the online journal.)

field of nine times larger area (red). These large area reference fields have also been used to measure the distances, magnitudes, and metallicities referred to later in this paper. For And XXIII, And XXIV, And XXV, and And XXVI, the reference regions are described by elliptical annuli with the same ellipticity and position angle of the dSph in question (see Table 1), the inner boundary lies at four half-light radii from the center of the dSph, and the outer boundary is positioned so that the area covered is

nine times larger (after allowing for gaps and edges) than the area used for the dSph. For And XXVII, a circular reference region was chosen 1° to the northeast to avoid the extended tidal stream as much as possible.

In Figure 3, only candidate RGB stars, which were selected from the regions marked with dashed red lines on the dwarf galaxy CMDs, are included in the LFs. The *i*-band LFs of the corresponding reference regions, normalized from a much larger area to reduce shot noise, are unable to match the shape and number overdensities due to the dSph galaxies. At bright magnitudes, the LFs peter out and eventually stop beyond $i \sim 21.0$. This marks the point (TRGB) where H-shell burning ceases and the He-flash is triggered. The *I*-band luminosity of the TRGB is almost independent of metallicity for dSph systems such as these (Bellazzini et al. 2001) and provides an excellent distance indicator for well-populated RGBs. However, since most of the new dSphs are relatively sparsely populated and the TRGB is not always well defined, we have based our primary distance estimate on the luminosity of the HB and indicated the predicted location of the TRGB with an arrow in Figure 3 (see Section 4.2).

And XXIII is the largest of the newly discovered dwarf galaxies. Given its size and stellar density, it may seem surprising that it has not been discovered before but even close inspection of the on-line digitized photographic plate sky surveys (e.g., http://archive.stsci.edu/cgi-bin/dss_form) shows nothing visible at this location. However, with central surface brightnesses of $\Sigma_{V,0} \approx 27.5$ (mag arcsec^{-2}) for all of these new discoveries (see Section 4.3 and Table 1), their invisibility on previous sky surveys is not unexpected.

The imaging of And XXV provides a good example of Murphy's law and also illustrates the pitfalls of surveys like this with emphasis on large area coverage and survey speed at the expense of filling all the gaps between detectors, and also sometimes field edges (see Figure 2). Much of And XXV falls in the ≈2 arcmin gap between the unbutted edges of two of the rows of nine CCDs making up part of the MegaCam array. The small amount of dithering in the (usual) three exposure dither sequence fills the tiny gaps between the long side of the detectors but does little for the much larger gap on either side of the outer short edges of the middle set of the 2 × 9 three-edge-buttable detectors. It is hardly surprising that gaps and edges make an appearance, even in this small sample of vignettes, since half of the surveyed region lies within ≈5–6 arcmin of either a field boundary or a large gap between rows of detectors. Fortunately, from a discovery viewpoint, most M31-distance dSphs are large enough to be found even in they land in the middle of a gap, while from a census standpoint, the impact of gaps on completeness is one of the several factors that can readily be quantified, but is outside the scope of this paper.

And XXIV and And XXVI have the most sparsely populated RGBs of the dSphs resulting in much noisier LFs. However, in both cases a metal-poor RGB sequence can still be clearly discerned, which is manifestly absent in the companion reference fields. And XXVI suffers somewhat for lying in a field with a much shallower limiting *i*-band and *g*-band depth (by ≈0.$^{\rm m}$5 and 0.$^{\rm m}$25 respectively) due to poorer than average seeing) compared to most of the other fields.

And XXVII is a unique case among these galaxies as it may be directly connected to an obvious stellar stream which it seems to form part of. In Figure 1, it can be seen to align with part of the great northwestern arc of stars, at least in projection. On the CMD, its stars have the same distribution of colors and magnitudes as stars selected from the arc implying that they have similar stellar populations and line-of-sight distances. This suggests the possibility that And XXVII is the partially disrupted remnant of a strong tidal disruption event. Since And XXVII is embedded in (or superimposed upon) an extended diffuse stream, it was difficult to find a clean comparison field in the near vicinity and it is likely that the handful of stars resembling an RGB in the references region (Figure 3) also belong to the stellar stream (and therefore, potentially, And XXVII).

4.1. Structural Properties

The structural parameters of And XXVIII–XXVII were determined by analyzing the spatial distribution of their resolved metal-poor candidate stars using a variant of the maximum likelihood technique developed by Martin et al. (2008, 2009), but in this case based on the Press–Schechter formalism (Schechter & Press 1976). The latter approach to likelihood problems such as this allows gaps in coverage to be directly assigned as window functions as an integral part of the analysis and therefore removes the requirement for artificially filling the gaps as part of an iterative solution.

Candidate stars used in the analysis are restricted to those used in the construction of the metal-poor distribution map shown in Figure 1. As in Martin et al. (2008), we use a simple elliptical exponential profile to describe the overdensity of stars in the galaxy, together with a constant background level. We differ further from their procedure by estimating the background level over a much larger region than used in the likelihood analysis and thereby fixing this parameter. These background levels are factored into the uncertainty estimates of the profile parameters but have no effect on the location parameters. This leaves six remaining parameters to be estimated. The central coordinates (α_o, δ_o), half-light radius (r_h), ellipticity ($\epsilon = 1 - b/a$, where a and b are the major and minor axes scale lengths of the system), and position angle (ϕ; measured east from north) are derived based on a simple grid search starting from visually determined initial estimates. The grid has step sizes of 0.05 in ϵ, 5° in ϕ, and 0.′05 in r_h. Providing that the starting central coordinates lie within the half-light core of the dSph, their exact value has no impact on the derived structural parameters because they are updated during the solution, and the likelihood surface is smoothly convex around the maximum value. The variation of the likelihood function over the grid also suffices to define the likelihood surface around the solution point for use in parameter error estimates (see, for example, Martin et al. 2008). Specifically, the uncertainties in the profile parameters are quoted as 1σ errors from direct analysis of the marginalized likelihood contours from the grid search.

The central overdensity, f_o, is effectively a nuisance parameter and is readily determined, given the other parameters, by iteratively solving the nonlinear equation $\partial ln\ L/\partial f_o = 0$. We note that in the Press–Schechter method this is not the same as using the integral constraint in Martin et al. (2008). The central coordinates were initially chosen by visual inspection of the overall survey map (which is constructed with an embedded Tangent Plane World Coordinate System) and then updated by using contoured isopleth maps of the central regions of each galaxy. From the viewpoint of their structural properties defined by r_h, ϵ, ϕ, the precise values of the central coordinates (α_o, δ_o) are of secondary importance and we found in practice that we could reduce the dimensionality of the grid search by updating these directly from the algebraic solutions of $\partial ln\ L/\partial \Delta\xi = 0$, $\partial ln\ L/\partial \Delta\eta = 0$, where $\Delta\xi$ and $\Delta\eta$ are the offsets in standard

coordinates (rotated to the best-fitting ellipse coordinate frame) from the current tangent point (α_o, δ_o) of the solution (see the Appendix for further details). After an iteration of the profile parameter grid search, the central coordinates are updated and the process repeated until a satisfactory convergence is achieved.

To construct the radial profile for display purposes, the average density of stars contained within fixed elliptical annuli and at a constant position angle was evaluated, and the profiles were corrected for foreground and/or background contamination using the (much larger) normalized reference region. Due to slight gradients in field contaminants the error in setting the background level is dominated by systematics as much as by Poisson noise. Because of this, as noted earlier, we decoupled the background determination by fixing the value in the maximum likelihood estimates of the other parameters and then directly explored the effects of plausible changes in this background level by re-running the estimator with a small range of background values.

The right-hand panels of Figure 2 show the background-corrected radial profiles derived from the metal-poor candidate spatial distributions, where the error bars include contributions from Poisson errors and the error in determining the local background level. The radial distributions shown for each galaxy were derived from average counts in elliptical annuli using the derived ellipticities and position angles, with due allowance for gaps in the survey coverage. We note that the exponential profile shown overlaid for each galaxy is not a direct fit to the binned data points but comes directly from the maximum likelihood analysis outlined earlier.

The gaps in coverage vary significantly for each galaxy, but even And XXV and And XXVI, the worst affected, are only missing ∼10% of their stellar populations and still allow reasonable best-fit parameters to be determined. And XXVII presents a different challenge since here the background model should be more complex than a simple constant level because of the intersecting tidal stream. The simple maximum likelihood method used above failed to converge in this instance because of the complex stream-like substructure in which And XXVII is embedded and we employed an alternative technique to derive the profile parameters. To determine ϵ and ϕ, we constructed a contoured isopleth map of the region around And XXVII and computed zeroth, first, and second moments of the surface density distribution, at a range of simple thresholds relative to the background (e.g., Irwin et al. 2005). This provided a well-defined ϕ but a relatively poorly defined ϵ due to the complexity of the stream-like distribution surrounding the core. Using the average values of ϵ and ϕ and the weighted center of gravity from the first moments, we then computed the radial elliptical profile (shown in Figure 2) and directly fitted an exponential profile to the inner 5 arcmin zone.

The derived parameters for all five galaxies are listed in Table 1. Interestingly, these new satellites span the complete range of parameters found previously in M31 dSphs. And XXIII has a particularly large half-light radius of $r_h = 1.04$ kpc. Only one other currently known dSph satellite companion of M31 has a larger half-light radius: And XIX which has $r_h = 1.7$ kpc. At the other extreme, And XXVI is the smallest of the new galaxies with $r_h = 0.23$ kpc and also among the smallest of the currently known M31 dSph population.

4.2. Distances

Most of the newly discovered dwarf galaxies are too poorly populated to directly determine their distances using traditional TRGB methods. The absence of sufficient numbers of stars near the tip of the RGB unsurprisingly leads to unreliable distance estimates (see Figure 3). Instead, we decided to use the extra depth of the g-band for bluer stellar populations to directly measure the luminosity of the horizontal branch (HB). This feature accounts for the strong overdensities sloping to fainter magnitudes and bluer colors at the bottom of the CMDs, e.g., from $g - i = 1.0, i = 24.5$ to $g - i = 0.0, i = 25.5$ on the CMD of And XXIII (Figure 3). The i-band depth cuts through this region precluding direct isochrone fitting, but we can still exploit the better depth of the g-band directly by analyzing the g-band LF instead.

As a benchmark, the HB magnitude of M31 is $g_0 = 25.2$, which in the typical extinction for this region translates to an apparent magnitude of $g = 25.4$–25.5. Since most of the g-band data we have extend down to at least $g = 26.5$ mag (and to between $g = 25.5$–26.0 with S/N = 10), we have a good chance of resolving the HBs of the new dSphs. However, not surprisingly, the comparison regions in the CMDs show that there is a notable component of contamination from unresolved background galaxies which necessitates a careful treatment of the background correction.

The observed g-band LFs of And XXIII–XXVII are shown in the left-hand panel of Figure 4 (black histograms) and those of the same appropriately scaled background reference fields (see Section 4) used for the i-band LFs are shown in red. Since the g-band data reach significantly deeper than the i-band for such stars, only a detection in the g-band is required, and the number of stars contributing to these LFs is much larger than for the equivalent i-band LFs. The right-hand panel of Figure 4 shows the g-band LF of each galaxy with the background-subtracted (black histogram) and a best-fit Gaussian (including a term to account for the sloping background of the LF) to the HB overplotted in red. The peak of the fits and corresponding rms errors for each galaxy are shown in Figure 4. The peak in the g-band luminosity corresponding to the HB varies from $g = 25.0$ mag to $g = 25.7$ mag. The rms error in the g-band magnitude over this range is ≈0.1 mag and the putative HB fits are generally well defined.

To ascertain the sensitivity of the HB estimates to completeness effects we have generated approximate completeness-corrected difference LFs using a generic form for the completeness as a function of point-source S/N. Full completeness tests are outside the scope of this paper, but we note that in comparable data sets the completeness level is better than 90% for 10σ fluxes and typically drops to ∼50% by 5σ. For the galaxies presented here, an S/N of 5σ occurs for g-band magnitudes of 26.0–26.3, where a steep falloff in the LF is observed in the comparison region. The approximate completeness-corrected difference LFs are plotted as gray histograms in the right-hand panels of Figure 4. They show that the HB is well resolved for And XXIII, And XXIV, And XXV, and And XXVI. For these galaxies, the number of stars reaches a clear peak (highlighted by the Gaussian fit) around the HB and drops down again before beginning to rise as the RGB progresses to fainter magnitudes. The best-fit Gaussians to the HB peaks of the completeness-corrected LFs differed from the original fits by $\leqslant$0.02 mag, corresponding to a maximum deviation in the final distances of 9 kpc, which is negligible compared to other uncertainties.

In the case of And XXVII, the completeness-corrected LF distorts the HB peak, although this is exacerbated by the difficulty of finding a clean nearby comparison region.

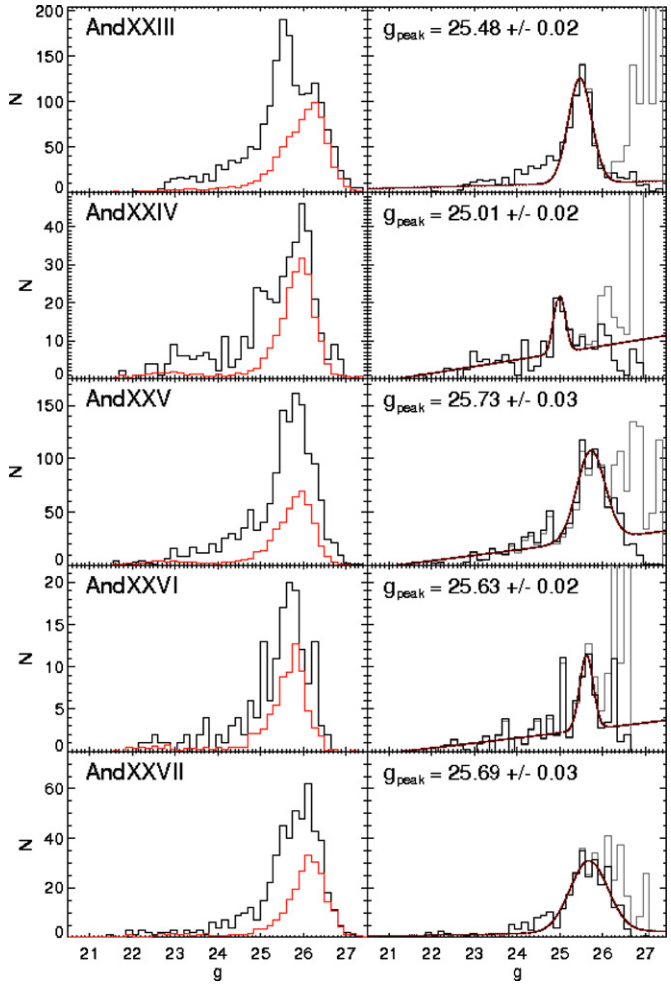

Figure 4. Left panels: the *g*-band luminosity functions of the central regions of each dwarf (black) together with suitably scaled much larger neighboring comparison regions (red). Right panels: difference luminosity functions (black) with simple Gaussian plus sloping background fits to the regions around the horizontal branches (red). An approximate completeness-corrected difference LF, as described in Section 4.2, is plotted in gray. The *g*-band magnitude of the peak of the fits is indicated together with an estimate of the rms error in the position of the peak.

(A color version of this figure is available in the online journal.)

Consequently, here we define a lower limit only for this galaxy. The peak of stars at $g = 25.5$ mag on the bottom right-hand panel of Figure 4 marks the brightest possible magnitude of the HB, and we use this to determine the lower limit on the distance.

To calculate the distance modulus, we must first estimate a standard absolute magnitude, M_g, for the HB populations typical of these dSphs. Empirical models which estimate the closely related M_V of the HB (e.g., Gratton 1998) have been predominantly determined from globular clusters and are shown to have a weak metallicity dependence (gradient). At the range of metallicities expected here, $-2.5 < [Fe/H] < -1.5$, the variation is less than $\pm 0.^m1$ which suggests a simple calibration based on similar dSphs which have independently determined reliable distances from TRGB measures and/or HB isochrone fits from *Hubble Space Telescope* data. To determine the value of the constant, we additionally measured the HB *g*-band luminosity of four relatively bright and well-studied dSphs (And I, And II, And III, and And XVI) which are covered by the PAndAS survey. The distance moduli of these well-populated dSphs, which have been determined using the TRGB method in previous papers, are 24.43 ± 0.07 (McConnachie et al. 2004), 24.05 ± 0.06 (McConnachie et al. 2004), 24.38 ± 0.06 (Da Costa et al. 2002), and 23.60 ± 0.20 (Ibata et al. 2007). Since these galaxies contain hundreds to thousands of RGB stars the rms errors in these measurements are small. Another reason for choosing these particular galaxies is because they tend to lie on the MW side of M31 and hence have clearly defined HBs in their *g*-band LFs. The formal rms error in locating their HB magnitudes is negligible (~0.02–0.03 mag) compared to the systematic errors due to the precise mix of their stellar populations

By comparing to the known distance moduli of And I, And II, And III and And XV, we find values for the absolute magnitude M_g of 0.89, 0.89, 0.79, and 0.67, respectively, and have therefore adopted a constant of $M_g = 0.8 \pm 0.1$ in the CFHT MegaCam AB magnitude system. These values are consistent, within the errors, with those derived for red HB stars by Chen et al. (2009) using Sloan Digital Sky Survey (SDSS) data for eight globular clusters with similar metallicities. The distances estimated by this method are dominated by the uncertainty of M_g, which in turn reflects uncertainties in the mix of blue-HB, red-HB, and red clump (RC) populations in these galaxies. Metallicity variation is most likely a secondary aspect given that all of the new objects have similar overall metallicities, [Fe/H] = −1.7 to −1.9, (see Section 4.4) to the calibrating objects ([Fe/H] = −1.5, −1.5, −1.9, and −1.7 from McConnachie et al. 2004; Da Costa et al. 2002; Ibata et al. 2007, respectively). Age effects will also influence the properties of the HB and RC, e.g., Girardi & Salaris (2001); however, given their appearance on the CMDs (Figure 3), it is highly unlikely that the newly discovered dSphs contain anything other than old, metal-poor stellar populations. To further refine these distance estimates deeper targeted imaging of sufficient depth to allow isochrone fitting to beyond the HB magnitude is required.

The distance moduli of the five new galaxies, after due allowance for line-of-sight reddening, are listed in Table 1. The errors in the distance moduli were calculated by propagating the error in M_g, the error in the measured location of the HB (see Figure 4), and the ±3% uncertainty in the calibration of the photometry. And XXIV lies the closest to the MW at 600 ± 33 kpc, And XXIII and XXVI lie at roughly the same line-of-sight distance as M31, 767 ± 44 kpc and 762 ± 42 kpc, respectively, while And XXV lies furthest from us, beyond M31, at 812 ± 46 kpc. The difficulty in measuring the HB magnitude of And XXVII means that we can only assign a lower limit to its distance of $\geqslant 757 \pm 45$ kpc.

As an independent consistency check, we have calculated the predicted magnitude of the TRGB in the *i*-band using our HB-based distance moduli and indicated them with an arrow in Figure 3. The estimated locations of the TRGBs of And XXIII–XXV agree well with the drop off in star counts at the bright end of their LFs. For And XXVI and And XXVII, the case is less clear due to the small numbers of stars, increasing the contamination from foreground stars from the overlapping "red cloud" region. To reliably disentangle dSph members from foreground stars in this part of the CMD requires spectroscopic followup (e.g., Letarte et al. 2009).

Further supporting evidence for the distances we have calculated is provided in the right-hand panels of Figure 5. Here, theoretical isochrones have been shifted to the derived distances and compared to the CMDs of the galaxies. In each case, the isochrones agree favorably with the distribution of the RGB stars.

4.3. Magnitudes

The absolute magnitudes (M_V) were computed by comparing the LFs of And XXIII–XXVII to the LFs of And I, And II, and And III. These latter dSphs are also part of the PAndAS survey and cover a similar range of metallicities and (presumably) mix of stellar populations. Absolute magnitudes of $M_V(\mathrm{And\,I}) = -11.8 \pm 0.1$, $M_V(\mathrm{And\,II}) = -12.6 \pm 0.2$, and $M_V(\mathrm{And\,III}) = -10.2 \pm 0.3$ were taken from McConnachie et al. (2004) and McConnachie & Irwin (2006a). For each dSph, background-subtracted g-band LFs were constructed using stars within loci such as those marked on the CMDs in Figure 3. All LFs are corrected for CCD gaps and include only stars within two half-light radii of the center of each galaxy using the structural parameters listed in Table 1 for the new dSphs and in McConnachie & Irwin (2006a) for the reference objects. Limiting the selection to two half-light radii includes roughly 85% of the flux and lessens the sensitivity to bright interlopers, but still leaves a shot-noise-dominated estimate at the bright end.

We then select the portion of the LFs containing all stars above the $\approx 90\%$ completeness level ($g < 25.5$ mag) and below an upper flux limit ($g > 22.5$ mag) for all eight dSphs. Assuming that the LFs are similar, the maximum likelihood scale factors that yield the best match between the new dwarfs and the reference set (And I, And II, and And III) define the difference in magnitude between the galaxies.

The variation in computed absolute magnitudes for each reference dSph gives some idea on the uncertainty introduced by assuming that the LFs of all of these galaxies are the same, when they may have different underlying stellar populations. Similarly, shifting the LFs by the maximum/minimum distance moduli allowed by our measurements in Section 4.2 gives a handle on the uncertainties introduced by the distances. As an example, the absolute magnitudes of And XXVI computed in this way range from -6.6 to -7.5 mag giving $M_V = 7.1 \pm 0.5$. The final absolute magnitudes we quote are the mean of each set of three results, and we estimate the error to be $\pm 0\overset{\mathrm{m}}{.}5$ based on the average scatter in the computed sets of absolute magnitudes. As a consistency check, we repeated the estimates using the i-band LFs computed in a similar way but covering the magnitude range $21.0 < i < 24.5$ and found results consistent to within ± 0.1 mag in all cases.

The derived absolute magnitudes of the new dwarfs are listed in Table 1 and range from $M_V = -10.2 \pm 0.5$ for And XXIII to $M_V = -7.1 \pm 0.5$ for And XXVI. These absolute magnitudes were then used in conjunction with the derived structural parameters to directly estimate the central surface brightnesses, $\Sigma_{V,0}$, of the galaxies, also listed in Table 1. All of the new dSphs have similar central surface brightnesses ranging from $\Sigma_{V,0} = 28.0\,\mathrm{mag\,arcsec^{-2}}$ for And XXIII to $\Sigma_{V,0} = 27.1\,\mathrm{mag\,arcsec^{-2}}$ for And XXV.

4.4. Metallicities

Metallicity distribution functions (MDFs) of And XXIII–XXVII are presented in the left-hand panels of Figure 5. We have used the Dotter et al. (2008) isochrones in the CFHT/MegaCam g, i system (A. Dotter 2010, private communication) to construct the MDFs so that no filter transformations were required. Specifically, the data are compared to a grid of isochrones with age = 12 Gyr, $[\alpha/\mathrm{Fe}] = 0.0$ and $-2.5 \leqslant [\mathrm{Fe/H}] \leqslant -0.5$, spaced in 0.1 dex steps, which have been reddened to match the data and shifted to the distance modulus we determined for each galaxy (the $E(B-V)$ and $(m-M)_0$ values used are listed in Table 1). The right-hand panels show how the resulting isochrones for metallicities of [Fe/H] = −2.5, −2.0, and −1.5 dex are compared with the RGB sequences of And XXIII–XXVII. The −2.5 dex and −1.5 dex isochrones bound the RGB and match its curvature and brightness well in all cases, providing further support for our distance estimates. Stars within two half-light radii of the central coordinates of each galaxy were included in the MDFs if they satisfied $21.0 < i < 24.0$ and were bounded by the −2.5 dex and −0.5 dex isochrones. Each star is assigned the metallicity of the nearest isochrone and a histogram of the resulting distribution of metallicities is constructed. The MDFs have been background-subtracted using a suitably scaled (larger area) reference field satisfying the same conditions.

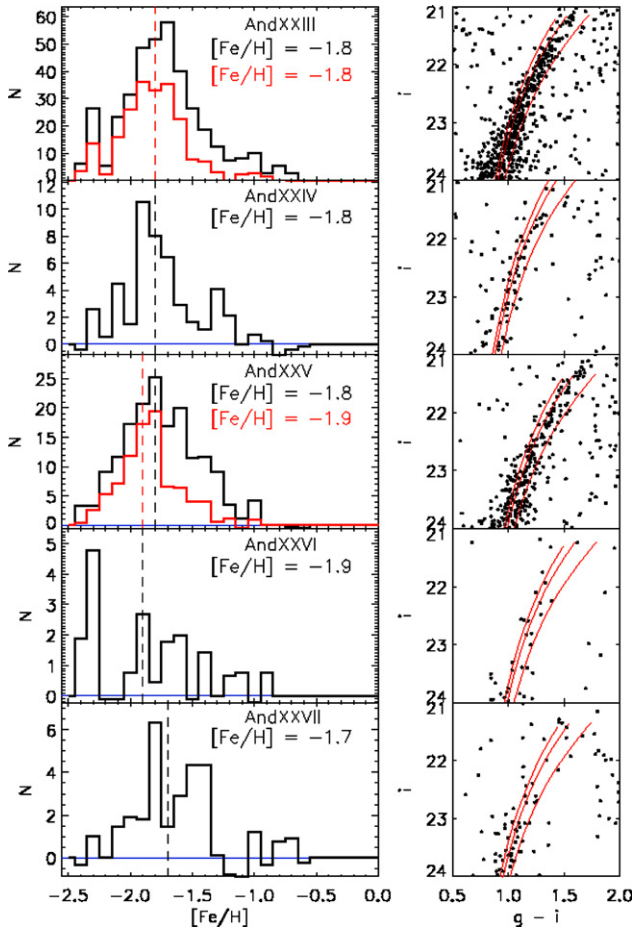

Figure 5. Left panels: metallicity distribution functions (MDFs) for And XXIII–XXVII derived assuming a fixed age of 12 Gyr an alpha-element enhancement of $[\alpha/\mathrm{Fe}] = 0.0$ and using the Dartmouth isochrone set (Dotter et al. 2008). Only stars within two half-light radii, with $21.0 < i < 24.0$, and colors bluer than the [Fe/H] = −0.5 dex isochrone were considered. A correction for background contamination was made using a suitably normalized (larger) nearby comparison region and the zero point is marked with a blue line. The median metallicity of each MDF is indicated by a dashed gray line. All of the dSphs have similar median metallicities ranging from [Fe/H] = −1.7 to [Fe/H] = −1.9 ±0.2. For the two most populated galaxies, And XXIII and And XXV, we have also derived the MDF of stars with $i \leqslant 23.0$ (red histograms) as a check on the impact of photometric errors. Right panels: a zoom-in section of the RGBs overlaid with Dotter et al. (2008) isochrones with age = 12 Gyr and metallicities of [Fe/H] = −2.5, −2.0, and −1.5 which have been shifted to the distance modulus calculated for each galaxy. The position of the isochrones is in very good agreement with the magnitude range and shape of the galaxy RGBs.

(A color version of this figure is available in the online journal.)

We have determined the median metallicity of each galaxy and marked it with a gray dashed line in Figure 5. Within the errors, all of the galaxies have the same median metallicity ranging from [Fe/H] $= -1.7 \pm 0.2$ dex to [Fe/H] $= -1.9 \pm 0.2$ dex. We note that the errors due to uncertainties in distance modulus have little impact on the upper part of the RGB for such low-metallicity systems. Re-deriving the metallicities of all five dSphs when the isochrones are shifted by ± 0.1 mag in distance modulus results in the change of median [Fe/H] by ∓ 0.1 dex. Altering the fiducial value of $[\alpha/\mathrm{Fe}]$ from 0.0 to 0.4 would systematically change their average [Fe/H] by -0.2 dex, while a $\pm 3\%$ photometric error in $g - i$ would result in a shift of ± 0.1 dex.

The MDFs of And XXIII and XXV, the two most populated galaxies, have very broad distributions (FWHM $\sim$0.5–0.8 dex). We caution that this should not be interpreted too literally as a large metallicity spread. Although there is some evidence at brighter magnitudes for a significant spread in the locus of the RGB for And XXIII and And XXV, for the more metal-poor isochrones, photometric errors, particularly at the faint end, contribute significantly to the spread in the derived MDF, and deeper targeted observations are needed to further investigate this. The red histograms in Figure 5 are the MDFs derived for And XXIII and And XXV when only stars brighter than $i = 23.0$ are considered. Both distributions, particularly that of And XXV, are somewhat narrower than before, but although photometric errors at fainter magnitudes contribute to broadening the MDF, they have little effect on the derived median [Fe/H] values. The sparseness of the RGB for the fainter dSphs makes it difficult to assess any spread in the locus, though we note that And XXIV has a particularly narrow spread of derived metallicities around its median value (FWHM = 0.3 dex), and is perhaps the galaxy with the clearest sign of having a simple stellar population. The MDFs of And XXVI and And XXVII are too noisy to make comparable inferences from their distributions.

5. DISCUSSION

5.1. Structural Properties

The five new dSphs have characteristics typical of the range of properties of the previously known M31 dSph population. The top panel of Figure 6 shows their location in the (semi-major axis) half-light radius vs. absolute magnitude plane together with the location of the other M31 dSph satellites and equivalent MW satellites satisfying $M_V \leqslant -4.5$. The values for the MW satellites Fornax, Leo I, Sculptor, Leo II, and Sextans were taken from Irwin & Hatzidimitriou (1995), while the parameters for the rest of the MW satellites were taken from Okamoto et al. (2008) and Okamoto (2010) and include the MW UFDs Boo I, Hercules, CVn I, CVn II, Leo IV, Leo T, and Uma I. The equivalent data for the previously known M31 satellites are from McConnachie & Irwin (2006a), Martin et al. (2006), Ibata et al. (2007), McConnachie et al. (2008), and Martin et al. (2009).

As expected, there is a general correlation between the size of the galaxy and its magnitude, though we caution that fainter than $M_V \approx -8$ observational selection effects may be limiting the detectability of larger half-light radii systems. The MW satellite population extends to fainter magnitudes than M31 satellites because, at the distance of M31, even relatively compact dwarf galaxies fainter than $M_V \approx -6$ are beyond our current detection limits. Although this rules out any direct constraints on putative UFDs around M31, it is interesting that the number of M31 satellites per absolute magnitude interval shows no sign of tailing off toward the faint end. This suggests that an equivalent population of UFDs is waiting to be discovered.

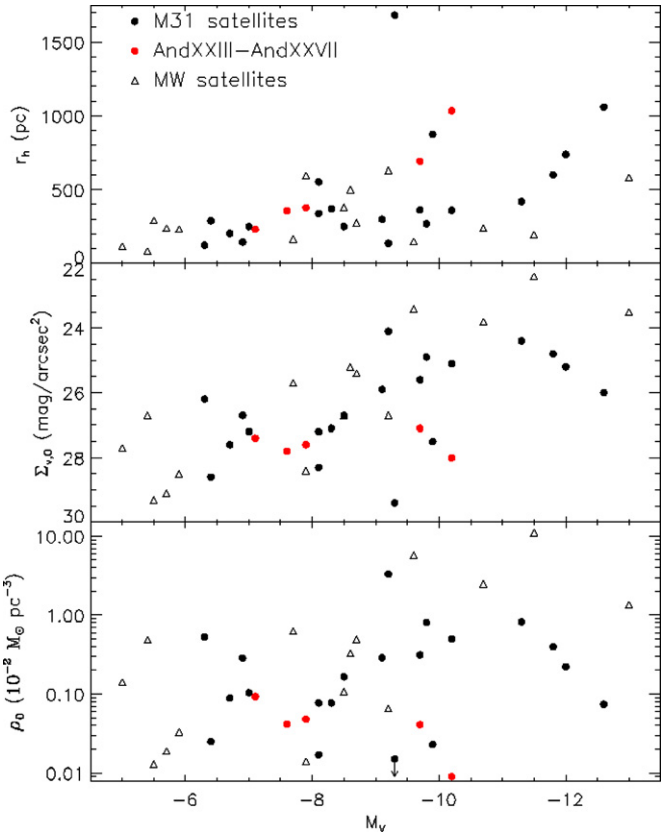

Figure 6. Top panel: the variation of half-light radius (r_h) with absolute magnitude (M_V) for the five newly discovered galaxies presented in this paper (red circles), other M31 satellites (black circles), and MW satellites (triangles). The source of the data is referred to in the text. Middle panel: the variation of central surface brightness ($\Sigma_{V,0}$) as a function of M_V. Values of $\Sigma_{V,0}$ have been taken from the literature where available, otherwise they have been estimated using r_h and M_V as described in Section 5.1. Bottom panel: the variation of inferred central luminosity density ρ_o as a function of M_V. And XIX has a value much lower than the plot boundary as indicated by the downward arrow. Note both the factor of 1000 variation in central luminosity (and implied baryon) density over the whole population and the factor of 10 difference in this quantity between the brighter ($M_V < -9.0$) M31 dSphs and their MW counterparts.

(A color version of this figure is available in the online journal.)

Following their analysis of the structural properties of And I–VII, McConnachie & Irwin (2006a) noted that the dwarf satellites of M31 tended to have larger radii than MW dwarf satellites and were typically twice as big. Subsequently, 18 new M31 dSphs (And XI–And XIII (Martin et al. 2006), And XIV (Majewski et al. 2007), And XV and And XVI (Ibata et al. 2007), And XVII (Irwin et al. 2008), And XVIII–XX (McConnachie et al. 2008), And XXI and And XXII (Martin et al. 2009)) and 10 new MW dSphs, including six with $M_V \leqslant -4.5$, have been discovered: CVn I (Zucker et al. 2006), Boo I (Belokurov et al. 2006), Hercules, CVn II, and Leo IV (Belokurov et al. 2007), and Leo T (Irwin et al. 2007). Recent work by Kalirai et al. (2010) found that there is a significant overlap between the M31 and MW satellite populations at the low-luminosity end ($L \lesssim 10^6\, L_\odot$).

Figure 6 includes data from the new M31 and MW satellite galaxies more luminous than $M_V = -4.5$ in addition to the previously known satellites and the newly discovered galaxies presented for the first time in this paper, And XXIII–XXVII. When the new data are included there is no clear difference in

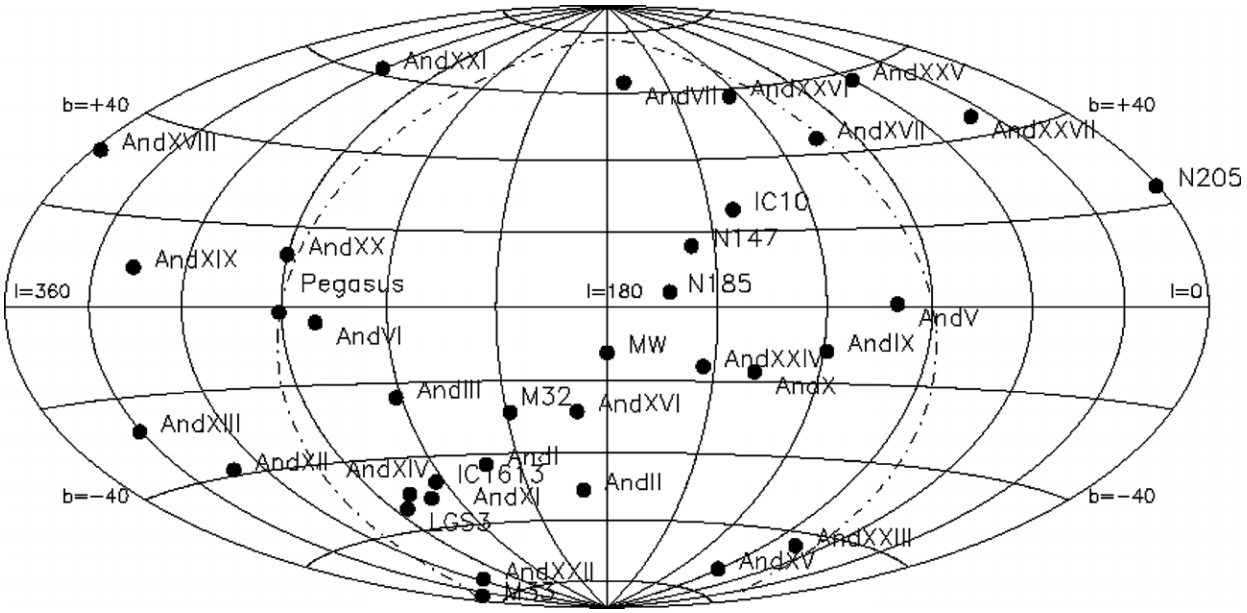

Figure 7. Aitoff projection of the all-sky distribution of the M31 satellite system as viewed from the center of M31. The coordinate system is defined using l_{M31} measured around the disk of M31 and locating the MW at $l_{M31} = 0^\circ$ and $b_{M31} = -12.^\circ5$ to account for the inclination of the M31 disk along the MW line of sight. The dot-dashed great circle centered on the MW splits the sky into MW near side and far side. With the extra M31 satellites now known, the earlier apparently significant asymmetry in the satellite distribution noted by McConnachie & Irwin (2006b) has now largely disappeared.

the M_V–r_h relation between MW and M31 satellites for absolute magnitudes fainter than $M_V \approx -9$. However, for the subset of dSph galaxies brighter than $M_V \approx -9$ it remains the case that the M31 dSph satellites are generally twice as extended as their MW counterparts, even though they are found at a similar range of distances (≈100–300 kpc) from their host galaxy. Of the new dSphs, the brighter pair, And XXIII and And XXV, continues this trend, whilst the three with $M_V > -9$ (And XXIV, And XXVI, and And XXVII) have half-light radii typical of both M31 and MW dSphs in this magnitude range. It is unlikely that this is a completeness issue since MW satellite galaxies brighter than $M_V = -9$ and with $r_h \geqslant 600$ pc should be easy to find if they lie within the expected distance range of MW satellites (e.g., Koposov et al. 2008).

As an alternative way of looking at these distributions, the variation of central surface brightness, $\Sigma_{V,0}$, as a function of half-light radius is shown in the middle panel of Figure 6. Fainter than $M_V \approx -9$, MW and M31 satellites show a similar range of central surface brightness. However, for those brighter than $M_V \approx -9$, M31 satellites have significantly fainter central surface brightness than their MW counterparts by an average of $\sim$2 mag arcsec^{-2}.

Finally, in the third panel of Figure 6, we make the plausible assumption that, to first order, we can deconvolve the projected surface density distribution by approximating it as a Plummer law (Plummer 1911) with the geometric mean half-light radius deduced from the parameters in Table 1. This allows us to analytically infer the equivalent central luminosity density and also, by effectively assuming a constant baryonic mass-to-light ratio, gain a measure of the variation of the central baryon density.

In M31, it appears that the brighter (classical) dSphs are not only twice as extended as their MW counterparts but also correspondingly have central stellar densities a factor of 10 smaller. This is a significant difference and suggests that the local environment around these two L_* galaxies has exerted a strong influence on the formation and evolution of these dSph systems.

In a study attempting to relate the observed properties of Local Group dSphs to their dark matter content, Peñarrubia et al. (2008) suggested that, under the assumption that M31 and MW satellites have similar dark matter halos, the systematic difference in their sizes should be complemented by a systematic difference in their kinematics. Specifically, they predicted that M31 satellites should have a velocity dispersion ∼50%–100% larger than the corresponding MW satellites. However, a recent kinematic survey of And I, And II, And III, And VII, And X, and And XIV by Kalirai et al. (2010) and similar work by Collins et al. (2010) have shown that this prediction is not borne out by observation. M31 satellites with measured velocity dispersions range from And X at $M_V = -8.1$ and $\sigma_v = 3.9 \pm 1.2$ km s^{-1} to And I at $M_V = -11.8$ and $\sigma_v = 10.6 \pm 1.1$ km s^{-1} (Kalirai et al. 2010). Meanwhile, MW satellites covering the same absolute magnitude interval have $\sigma_v = 9.5 \pm 2.0$ km s^{-1} (Draco at $M_V = -8.3$) to $\sigma_v = 10.5 \pm 2.0$ km s^{-1} (Fornax at $M_V = -13.0$) according to Mateo (1998). This suggests, as also noted by Peñarrubia et al. (2008), that the nature of the dark matter halos themselves may be responsible for the observed differences between the two satellite systems.

5.2. Satellite Spatial Distribution

An interesting peculiarity in the M31 satellite distribution noted by McConnachie & Irwin (2006b) was the tendency for the then known satellites of M31 to be preferentially located on the MW side of M31 (14 out of 16). With the discovery of 18 more M31 satellites since then it is worth revisiting the satellite distribution again. As before, we define an M31-centric coordinate system such that the disk of M31 defines the galactic plane, i.e., latitude $b_{M31} = 0^\circ$, and such that the MW lies at longitude $l_{M31} = 180^\circ$ and latitude $b_{M31} = -12.^\circ5$. Within this coordinate system the distribution of M31 satellites, as would be seen from the center of M31, is shown in the Aitoff projection of Figure 7. The outlined great circle has a pole centered on the MW position and splits the M31 sky into those objects lying on the MW side within, and on the opposite side to the MW,

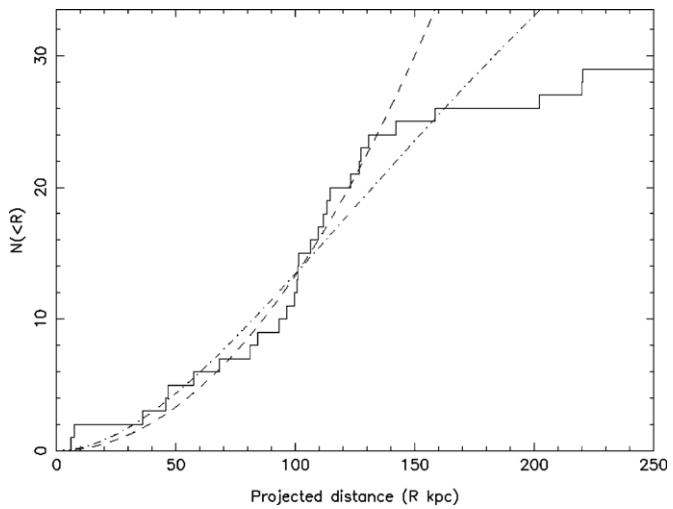

Figure 8. Cumulative distribution of the number of satellite galaxies as a function of the projected distance from M31. The overlaid models are: a power-law distribution of the form $\rho(r) \propto r^{-\alpha}$ with $\alpha = 1$ (dashed line) and an Einasto density distribution with $\alpha = 0.678$ and $r_{-2} = 200$ kpc (e.g., Springel et al. 2008; dot-dashed line). Note particularly that the power-law model corresponds to a constant surface density of satellites and that the clear break in the projected cumulative profile at the main PAndAS survey limit of ≈150 kpc suggests a large number of satellites remain to be discovered further out. The cosmologically motivated model does not provide a good fit to the observed surface density distribution.

without. Although there is still an apparent bias, with 24 out of 34 satellites lying on the MW side of M31, the offset in the line-of-sight distance distribution is much less significant than that shown in Figure 8 of McConnachie & Irwin (2006b). With the additional satellites, and updated information for the rest, the median offset toward the MW changes from 40 kpc to 21 kpc, and changes from a 3σ bias to less than a 2σ event.

On the other hand, the overall spatial distribution of the satellites of M31 reveals an unexpected result. The projected (surface) spatial distribution of satellites depicted in Figure 8 highlights the visual impression commented on previously from the two-dimensional overview of satellite locations seen in Figure 1. Until the main limit of the current PAndAS survey is reached at a projected distance of ≈150 kpc from M31, there is an essentially uniform surface density of satellite galaxies as first pointed out by McConnachie et al. (2009). The turnover near 150 kpc in the projected cumulative distribution corresponds precisely to the limit of the main PAndAS survey. Since we know from their three-dimensional distribution that M31 satellites exist at distances up to at least 300–400 kpc from M31, it is quite likely that even with the current PAndAS survey we are still seriously incomplete in our census of even the relatively bright ($M_V \lesssim -7$) satellites.

In compiling this figure, we have included all suspected Andromedan satellites irrespective of their location relative to our currently surveyed region. The inclusion, or otherwise, of marginal Andromedan members such as And XVIII, makes little difference to the conclusion. The surprising result is that out to our approximate survey limit at ≈150 kpc in projection, the surface density of satellites is essentially constant. This corresponds to a three-dimensional radial density distribution, $\rho(r) \propto r^{-1}$, a result seemingly in conflict with cosmological simulations. As a particular example of one of these, we show in Figure 8 a standard cosmological model prediction of sub-halo density profiles based on an Einasto radial density distribution with parameters $\alpha = 0.678$ and $r_{-2} = 200$ kpc, taken from Figure 11 of Springel et al. (2008). Since the normalization here is arbitrary, both overlaid models were normalized to have the same mean projected surface density as observed out to 100 kpc. A constant surface density to ≈150 kpc in projection provides a reasonable description of the observed satellite population, whereas the cosmologically motivated model has a much steeper radial density falloff and a correspondingly much flatter predicted cumulative surface density distribution.

The present observed distribution of dwarf satellite galaxies will undoubtedly have been influenced by their range of orbital properties and evolutionary histories, with tidal effects preferentially destroying systems closer to the nucleus of M31. While we might expect that the original distribution of recognizable satellites could have been more centrally concentrated, the evolution over time of the distribution, and properties, of the surviving systems is less obvious. Although detailed simulations of the distribution of dark matter sub-halos have been made, the problem of accurately linking the surviving sub-halos with the observed satellite systems still remains (e.g., Ludlow et al. 2010).

6. SUMMARY

We have presented for the first time a panoramic view of metal-poor stars in the M31 halo out to an average projected radius of ∼150 kpc using data obtained with the MegaPrime/MegaCam wide-field camera on the CFHT during the PAndAS survey. Dwarf satellite galaxies and tidal debris streams have been discovered out to the edge of the survey, suggesting that much more is to be found at still larger radii. The degree of substructure visible in the overall map highlights the continuing growth and evolution of the outer halo and disk of M31 and yields an insight into the accretion process of an L_* disk galaxy.

In the main part of the paper we have characterized the five most recently discovered dSph galaxies uncovered by PAndAS, Andromeda XXIII–XXVII. They all contain stellar populations typical of dSph galaxies, with no obvious sign of substructure, a relatively narrow RGB and have mean metallicities ranging from [Fe/H] $= -1.7 \pm 0.2$ dex to [Fe/H] $= -1.9 \pm 0.2$ dex. Although the central surface brightnesses of the galaxies are broadly similar ($\Sigma_{v,0} = 27.5 \pm 0.5$ mag arcsec^{-2}, they vary in absolute magnitude ($M_V = -7.1 \pm 0.5$ to -10.2 ± 0.5) and have very different scale lengths ($R_h = 230$–1035 pc). These additional discoveries continue the trend whereby the brighter M31 dSphs have significantly larger half-light radii than their MW counterparts.

1. *And XXIII* is a bright ($M_V = -10.2$) satellite galaxy lying at the same line-of-sight distance as its host and ∼126 kpc away from it. With a half-light radius of $r_h = 1035$ pc, it is one of the largest of M31s presently known satellites and almost twice as extended as the largest known MW dSph satellite (Fornax: $r_h = 636$ pc; Irwin & Hatzidimitriou 1995).
2. *And XXIV and XXVI* resemble the traditional dSphs belonging to the MW group in many ways. They have small half-light radii ($r_h = 357$ pc and 232 pc) and are relatively faint ($M_V = -7.6 \pm 0.5$ and -7.1 ± 0.5). Both galaxies are very sparsely populated (see Figures 2 and 3). Our line-of-sight distance measurements show that both galaxies lie on the near side of M31 relative to the MW and, at a distance of 600 ± 33 kpc, And XXIV is one of the closest M31 dSphs to us.

3. *And XXV* has the typical characteristics of M31's dSph satellite system in that it is large ($r_h = 693$ pc) and bright ($M_V = -9.7$). It has the highest central surface brightness of the newly discovered galaxies ($\Sigma_{V,0} = 27.1$ mag arcsec^{-2}), still not bright enough to have been found by previous shallower surveys such as the SDSS.
4. *And XXVII* appears to be in the process of being tidally disrupted by M31. It is embedded in a great northern arc of stars which loops around M31. The stream of stars surrounding the galaxy has made it very difficult to extract a clean reference field to characterize the properties of the foreground and/or background. Of the five galaxies presented in this paper, And XXVII is furthest from the MW ($\sim$827 $\pm$ 47 kpc) and the nearest to M31 ($R_{M31} \sim$ 86 kpc).

Finally, we revisited the spatial distribution of the overall M31 satellite population and demonstrated that the apparent bias in the satellite location with respect to the MW noted by McConnachie & Irwin (2006b) has gradually disappeared with the discovery of more satellites. However, in recompense, the newly discovered satellites now allow an almost complete census out to a projected distance of $\approx$150 kpc and show a surprising uniformity of their surface density out to this limit. This not only suggests that a large fraction of the M31 satellite population remains to be discovered, but also that the three-dimensional radial density distribution of M31 satellites varies approximately as $\rho(r) \propto r^{-1}$ out to at least 150 kpc. It will be enlightening to compare this result with more detailed cosmological simulations based on the estimated numbers of surviving satellites of L_* galaxies. Surveying to comparable depths to beyond the virial radius of M31 ($\approx$250 kpc) is probably impractical with MegaCam but well within the capabilities of the upcoming Hyper-Suprime Cam on Subaru (Miyazaki et al. 2006) and would correspondingly provide a more exacting test of cosmological predictions.

We thank Sidney Van Den Bergh for a careful reading of the manuscript and for his helpful comments on the content. Thanks also to the entire staff at CFHT for their great efforts and continuing support throughout the PAndAS project.

APPENDIX

FITTING SURFACE PROFILES

We want to estimate the likelihood of observing the data points at position vectors $\{\mathbf{r_i}\}$ $i = 1, 2, \ldots, m$, where $f(\mathbf{r})$ is the surface density profile of a given dwarf galaxy superimposed on a uniform local background. Following the Press–Schechter formalism (Schechter & Press 1976), imagine partitioning the observed region into "cells" of the surface area δS. Let the expected number of observed data points in cell i be ϕ_i, where

$$\phi_i = f(\mathbf{r_i})\, \delta S, \tag{A1}$$

then the probability of observing x_i points in cell i is given by a Poisson distribution

$$P(x_i) = e^{-\phi_i}\, \frac{\phi_i^{x_i}}{x_i\,!}, \tag{A2}$$

and therefore the likelihood function for the ensemble of data points in the region is

$$L = \prod_i P(x_i) = \prod_i e^{-\phi_i}\, \frac{\phi_i^{x_i}}{x_i\,!}. \tag{A3}$$

Let $\delta S \to 0$, then $x_i = 1$ if a point is observed at this location, or $x_i = 0$ if none are detected. The likelihood function now becomes

$$L = \prod_i e^{-\phi_i}.\ \prod_i \phi_i\, e^{-\phi_i}, \tag{A4}$$

where the first product is over empty cells and the second is over occupied cells. Taking natural logarithms this further simplifies to

$$ln\ L = \sum_i -\phi_i + \sum_{i=1}^{m} ln\ \phi_i, \tag{A5}$$

where the first summation is now over all cells and the second only occupied cells. Since $\delta S \to 0$, we can replace the first summation with a surface integral over the region such that

$$ln\ L = -\int_S f(\mathbf{r})\, dS + \sum_{i=1}^{m} ln\ f(\mathbf{r_i}). \tag{A6}$$

Unobservable regions due to gaps, etc., are trivially included in the normalizing integral by use of a window function, which of course has no impact on the discrete summation of observed data points.

To illustrate the use of this method, we model the dSph as an ellipse with ellipticity ϵ, position angle θ in a standard coordinate grid, and use an exponential profile of scale length a along the major axis. In this case

$$f(\mathbf{r_i}) = f_o\, e^{-r_i/a} + b, \tag{A7}$$

where using standard coordinates $\Delta\xi$ and $\Delta\eta$ to denote offsets from the center of the dSph, i.e., $\xi - \xi_o$ and $\eta - \eta_o$, we have

$$r_i^2 = (\Delta\xi_i\ \cos\theta + \Delta\eta_i\ \sin\theta)^2 + (-\Delta\xi_i\ \sin\theta + \Delta\eta_i\ \cos\theta)^2/(1-\epsilon)^2. \tag{A8}$$

If the area for analysis, A, covers sufficient ellipse scale lengths, and there are no gaps in the coverage, then

$$ln\ L = -2\pi f_o\, a^2(1-\epsilon) - bA + \sum_{i=1}^{m} ln\ (f_o\, e^{-r_i/a} + b) \tag{A9}$$

and for a given trial grid solution for a, ϵ, θ, and for a particular background b, the central density f_o is defined by

$$\frac{\partial ln\ L}{\partial f_o} = 0 = -2\pi a^2(1-\epsilon) + \sum_{i=1}^{m} \frac{e^{-r_i/a}}{f_o\, e^{-r_i/a} + b}, \tag{A10}$$

which has a straightforward iterative solution for f_o. Likewise the central coordinates of the dSph, in a coordinate system rotated for convenience to lie along the major and minor axes, ξ_o', η_o', are defined by

$$\frac{\partial ln\ L}{\partial \xi_o'} = 0 = \sum_{i=1}^{m} \frac{\xi_i' - \xi_o'}{r_i\, a}\, \frac{f_o\, e^{-r_i/a}}{f_o\, e^{-r_i/a} + b}, \tag{A11}$$

which implies that

$$\xi_o' = \sum_{i=1}^{m} \frac{f_o\, e^{-r_i/a}}{f_o\, e^{-r_i/a} + b}\, \frac{\xi_i'}{r_i} \Big/ \sum_{i=1}^{m} \frac{f_o\, e^{-r_i/a}}{f_o\, e^{-r_i/a} + b}\, \frac{1}{r_i}, \tag{A12}$$

i.e., a simple weighted sum over the coordinates, with a similar solution for η'_o.

For numerical stability in solving the latter equation, we introduce a softening parameter in the core of the dSphs $r_i^2 \rightarrow r_i^2 + c^2$, where c is fixed to be equivalent to a 20 pc scale length. This also makes some allowance for the often observed flattening of the inner profile of dSphs with respect to a pure exponential.

REFERENCES

Bellazzini, M., Ferraro, F. R., & Pancino, E. 2001, ApJ, 556, 635
Belokurov, V., et al. 2006, ApJ, 647, L111
Belokurov, V., et al. 2007, ApJ, 654, 897
Chapman, S. C., et al. 2007, ApJ, 662, L79
Chen, Y. Q., Zhao, F., & Zhao, J. K. 2009, ApJ, 702, 1336
Collins, M. L. M., et al. 2010, MNRAS, 407, 2411
Da Costa, G. S., Armandroff, T. E., & Caldwell, N. 2002, AJ, 124, 332
Dotter, A., Chaboyer, B., Kostov, V., Jevermovíc, D., Baron, E., & Ferguson, J. W. 2008, ApJS, 178, 89
Evans, N. W., & Wilkinson, M. I. 2000, MNRAS, 316, 929
Ferguson, A. M. N., Irwin, M. J., Ibata, R. A., Lewis, G. F., & Tanvir, N. R. 2002, AJ, 124, 1452
Girardi, L., & Salaris, M. 2001, MNRAS, 323, 109
Gratton, R. G. 1998, MNRAS, 296, 739
Grcevich, J., & Putman, M. E. 2009, ApJ, 696, 385
Ibata, R., Irwin, M., Lewis, G., Ferguson, A. M. N., & Tanvir, N. 2001, Nature, 412, 49
Ibata, R., Martin, N. F., Irwin, M., Chapman, S., Ferguson, A. M. N., Lewis, G. F., & McConnachie, A. W. 2007, ApJ, 671, 1591
Irwin, M. J., Ferguson, A. M. N., Huxor, A. P., Tanvir, N. R., Ibata, R. A., & Lewis, G. F. 2008, ApJ, 676, L17
Irwin, M., Ferguson, A. M. N., Ibata, R. A., Lewis, G., & Tanvir, N. 2005, ApJ, 628, L105
Irwin, M., & Hatzidimitriou, D. 1995, MNRAS, 277, 1354
Irwin, M., & Lewis, J. 2001, New Astron. Rev., 45, 105
Irwin, M. J., et al. 2007, ApJ, 656, L13
Johnston, K. V., Hernquist, L., & Bolte, M. 1996, ApJ, 465, 278
Kalirai, J. S., et al. 2010, ApJ, 711, 671
Koposov, S., et al. 2008, ApJ, 686, 279
Letarte, B., et al. 2009, MNRAS, 400, 1472
Ludlow, A., Navarro, J. F., Springel, V., Vogelsberger, M., Wang, J., White, S. D. M., Jenkins, A., & Frenk, C. S. 2010, ApJ, 692, 931
Mackey, A. D., et al. 2010, ApJ, 717, L11
Majewski, S. R., et al. 2007, ApJ, 670, L9
Martin, N. F., de Jong, J. T. A., & Rix, H.-W. 2008, ApJ, 684, 1075
Martin, N. F., Ibata, R. A., Irwin, M. J., Chapman, S., Lewis, G. F., Ferguson, A. M. N., Tanvir, N., & McConnachie, A. W. 2006, MNRAS, 371, 1983
Martin, N. F., et al. 2009, ApJ, 705, 758
Mateo, M. L. 1998, ARA&A, 36, 435
McConnachie, A. W., & Irwin, M. J. 2006a, MNRAS, 365, 1263
McConnachie, A. W., & Irwin, M. J. 2006b, MNRAS, 365, 902
McConnachie, A. W., Irwin, M. J., Ferguson, A. M. N., Ibata, R. A., Lewis, G. F., & Tanvir, N. 2004, MNRAS, 350, 243
McConnachie, A. W., Irwin, M. J., Ferguson, A. M. N., Ibata, R. A., Lewis, G. F., & Tanvir, N. 2005, MNRAS, 356, 979
McConnachie, A. W., et al. 2008, ApJ, 688, 1009
McConnachie, A. W., et al. 2009, Nature, 461, 66
Miyazaki, S., et al. 2006, Proc. SPIE, 6269, 9
Okamoto, S. 2010, PhD thesis, Univ. Tokyo
Okamoto, S., Arimoto, N., Yamada, Y., & Onodera, M. 2008, A&A, 487, 103
Peñarrubia, J., McConnachie, A. W., & Navarro, J. F. 2008, ApJ, 672, 904
Plummer, H. C. 1911, MNRAS, 71, 460
Schechter, P., & Press, W. 1976, ApJ, 203, 557
Schlegel, D. J., Finkbeiner, D. P., & Davis, M. 1998, ApJ, 500, 525
Springel, V., et al. 2008, MNRAS, 391, 1685
Tanaka, M., Chiba, M., Komiyama, Y., Guhathakurta, P., Kalirai, J. S., & Iye, M. 2010, ApJ, 708, 1168
Zucker, D. B., et al. 2004, ApJ, 612, L121
Zucker, D. B., et al. 2006, ApJ, 643, L103
Zucker, D. B., et al. 2007, ApJ, 659, L21